Microsc. Microanal. 19, 1669–1677, 2013
doi:10.1017/S1431927613013317

Microscopy AND Microanalysis

Three-Dimensional Chemical Mapping by EFTEM-TomoJ Including Improvement of SNR by PCA and ART Reconstruction of Volume by Noise Suppression

Cédric Messaoudi,[1,2] Nicolas Aschman,[1,2] Marcel Cunha,[1,2,†] Tetsuo Oikawa,[3] Carlos O. Sanchez Sorzano,[4] and Sergio Marco[1,2,*]

[1]*Institut Curie, Centre de Recherche, Bat 112, Centre Universitaire, 91405 Orsay Cedex, France*
[2]*INSERM U759, Bat 112, Centre Universitaire, 91405 Orsay Cedex, France*
[3]*JEOL Ltd., 1-2 Musashino 3-chome, Akishima, Tokyo 196-8558, Japan*
[4]*National Center of Biotechnology (CSIC), c/Darwin, 3. Campus Univ. Autónoma de Madrid, 28049 Cantoblanco, Madrid, Spain*

Abstract: Electron tomography is becoming one of the most used methods for structural analysis at nanometric scale in biological and materials sciences. Combined with chemical mapping, it provides qualitative and semiquantitative information on the distribution of chemical elements on a given sample. Due to the current difficulties in obtaining three-dimensional (3D) maps by energy-filtered transmission electron microscopy (EFTEM), the use of 3D chemical mapping has not been widely adopted by the electron microscopy community. The lack of specialized software further complicates the issue, especially in the case of data with a low signal-to-noise ratio (SNR). Moreover, data interpretation is rendered difficult by the absence of efficient segmentation tools. Thus, specialized software for the computation of 3D maps by EFTEM needs to include optimized methods for image series alignment, algorithms to improve SNR, different background subtraction models, and methods to facilitate map segmentation. Here we present a software package (EFTEM-TomoJ, which can be downloaded from http://u759.curie.fr/fr/download/softwares/EFTEM-TomoJ), specifically dedicated to computation of EFTEM 3D chemical maps including noise filtering by image reconstitution based on multivariate statistical analysis. We also present an algorithm named BgART (for background removing algebraic reconstruction technique) allowing the discrimination between background and signal and improving the reconstructed volume in an iterative way.

Key words: EFTEM, electron tomography, 3D reconstruction, chemical mapping

Introduction

Energy-filtered transmission electron microscopy (EFTEM) allows the computation of qualitative elemental maps describing the spatial distribution of chemical elements in the analyzed samples. EFTEM maps are images calculated from a fraction of inelastically scattered electrons coming from the studied elements after removing unspecific signals. While the information provided by such two-dimensional (2D) maps is certainly useful; as 2D maps are projections of 3D objects, they are incapable of truthfully representing the chemical distribution within these objects. Presently, the 3D structure of an object can be obtained by transmission electron tomography, which involves the computational combination of projection images acquired at different angles around a tilt axis. Transmission electron tomography is commonly used to obtain structural information of several types of samples analyzed by transmission electron microscopy (TEM). Transmission electron tomography can be combined with EFTEM in order to generate 3D chemical maps and thus overcome the limitations of 2D maps.

Received February 13, 2013; accepted July 16, 2013
**Corresponding author*. E-mail: sergio.marco@curie.fr
[†]Current address: Departamento de Biologia Celular, Instituto de Biologia Roberto Alcantara Gomes, Universidade do Estado do Rio de Janeiro, Brazil

A major obstacle in obtaining 3D maps from EFTEM data is the lack of dedicated software that provides and combines the specific methods required at each step in the computation of accurate elemental maps. More specifically, this concerns: (i) truthful registration of images acquired at the same tilt angles but different energies; (ii) choice of different mathematical functions to model the background signal in order to extract the elemental signal; (iii) accurate approaches for signal-to-noise ratio (SNR) improvement; and (iv) volume–background suppression. As a consequence, combining transmission electron tomography with EFTEM to get 3D chemical maps is recent and examples in the literature are few. In materials sciences, the first successful attempts to compute 3D-EFTEM were done in 2001 on the nanocomposite FeAl + Y_2O_3 (Möbus & Inkson, 2001), while in the biological sciences, after an initial work on inorganic structures (magnetite crystals) in magnetotactic bacteria (Midgley & Weyland, 2003), the first studies on organic structures concern the analysis of phosphorus concentration using unstained sections of cells. This was performed on *Caenorhabditis elegans* ribosomes (Leapman et al., 2004; Aronova et al., 2007) or nuclear chromatin (Aronova et al., 2010) allowing sensitivities up to 20 phosphorus atoms in a 2.7 nm-sized voxel. One of these works (Aronova et al., 2007) demonstrates the feasibility of quantitative

electron spectroscopic tomography and proposes a tool, written in MATLAB and FORTRAN, to compute quantitative phosphorous 3D maps. Previously, a software package dedicated to general EFTEM tomography was published (Boudier et al., 2005) implementing a basic set of algorithms for 3D chemical mapping such as the three-window method of background subtraction. This method consists of estimating the background contribution to the element-specific signal by extrapolation from two images recorded with inelastic electrons below the energy-loss edge of the element of interest. However, in order to generate accurate 3D elemental maps and to make EFTEM more widely accessible, we deemed it necessary to extend this basic approach. This could be done by multivariate statistical analysis (MVA), which has been shown to improve SNR before computing 2D elemental maps (Quintana et al., 1998; Lozano-Perez et al., 2009) or EELS spectra (Yedra et al., 2012). Another way would be to introduce known information about the signal during the iterative algebraic reconstruction technique (ART) process as done by algorithms such as discrete algebraic reconstruction technique (DART) (Batenburg & Sijbers, 2011; Goris et al., 2013). Such improvements would ideally be combined with robust fiducial-less image registration algorithms (Sorzano et al., 2009), flexibility in the choice of functions for background modeling, and a user-friendly interface.

We chose to implement all of these possibilities in a plugin for ImageJ (Schneider et al., 2012) due to the widespread use of this software by the microscopy community as well as its ease of installation and cross-platform compatibility. The software also includes a new algorithm called BgART (for background removing algebraic reconstruction technique), which discriminates between pixels belonging to the reconstructed object of interest and the background during the ART reconstruction process.

Materials and Methods

Developments and computations were performed using a computer equipped with an i7-2820QM processor at 2.3 GHz. Software and interface for EFTEM were developed for the Java platform as an independent ImageJ plugin. The BgART algorithm was integrated in the ImageJ tomographic reconstruction plug-in TomoJ (Messaoudi et al., 2007). After testing implementation with phantoms, the method was applied on experimental data collected from a biological specimen. Briefly, samples of the unicellular fungus *Fonsecaea pedrosoi* (Cunha et al., 2005) were treated with cationized ferritin in order to detect anionic areas on the cell wall by visualizing the distribution of iron. These experimental data consisted in tomographic tilt series acquired, using a Saxton scheme from $-60°$ to $60°$ with TEMography Software from JEOL Ltd. (Tokyo, Japan), using a JEOL2200FS electron microscope equipped with an in column omega-filter at electron energy-loss values of 560, 590, 620, 650, 680, and 710 eV with an energy window of 20 eV. *F. pedrosoi* samples were prepared from 5-day-old cultures filtered in a 40–60 G porous plate filter followed by centrifugation (13,600 $\times$ *g*, 30 min, 4°C) to isolate the conidial forms. Fungal conidia were fixed with 2.5% glutaraldehyde in PBS, exhaustively rinsed with PBS, and incubated in the presence of 10 μg/mL cationized ferritin, at pH 7.2, for 1 h at room temperature. Cells were postfixed for 30 min in 1% osmium tetroxide, dehydrated in acetone, and embedded in Epon. Sections of 150 nm thickness were used for observation.

After ART reconstruction using TomoJ (50 iterations and 0.1 for relaxation coefficient), evaluation of the performance of MVA and BgART on experimental data was done by calculating SNR in three regions of interest (ROI) corresponding to: resin (considered as background), cytoplasm (where iron is not cumulated), and electron dense aggregates at the fungus cell wall (corresponding to iron accumulations).

SNR was calculated in decibels using the standard definition:

$$\mathrm{SNR} = 10 \log_{10}\left(\frac{A_s}{A_b}\right)^2,$$

where A_s is the amplitude of the net signal, computed as the average pixel intensity in the analyzed ROI subtracted by the average pixel intensity in the resin ROI, whereas A_b is the amplitude of the background estimated by the standard deviation calculated at the resin ROI.

The SNR estimation has been done on the central section of the iron 3D maps computed: (i) without MVA or BgART; (ii) after MVA and image reconstitution using eigenvectors 1 and 6 obtained by principal component analysis (PCA); and (iii) after applying the procedure described in (ii) followed by BgART.

Results

To facilitate the computation of chemical maps, the graphical user interface of EFTEM-TomoJ was designed with separate panels corresponding to each of the major steps in the process, which allows for a sequential but reversible workflow (Fig. 1). The user can select and load the desired energy-loss tilt series, including *Z* loss, which should be grouped in a single directory. In the case of images collected on a JEOL microscope, EFTEM-TomoJ directly reads energy loss and window width information from the data file; otherwise this information needs to be entered by the user. The subset of images used for the computation of maps may be changed at any time during the process.

Because it is crucial that images acquired at the same tilt angles but different energies are correctly registered, we have implemented different tools for automatic energy-loss image alignment based on multiscale methods (Bonnet & Liehn, 1988) with cross-correlation, mean square difference, and mutual information (Pluim et al., 2003) as possible scoring functions. In addition, the user can choose which energy-loss tilt series will be used as a reference. Finally, a manual alignment interface is also offered including tools for visual evaluation of the alignment by color superimpo-

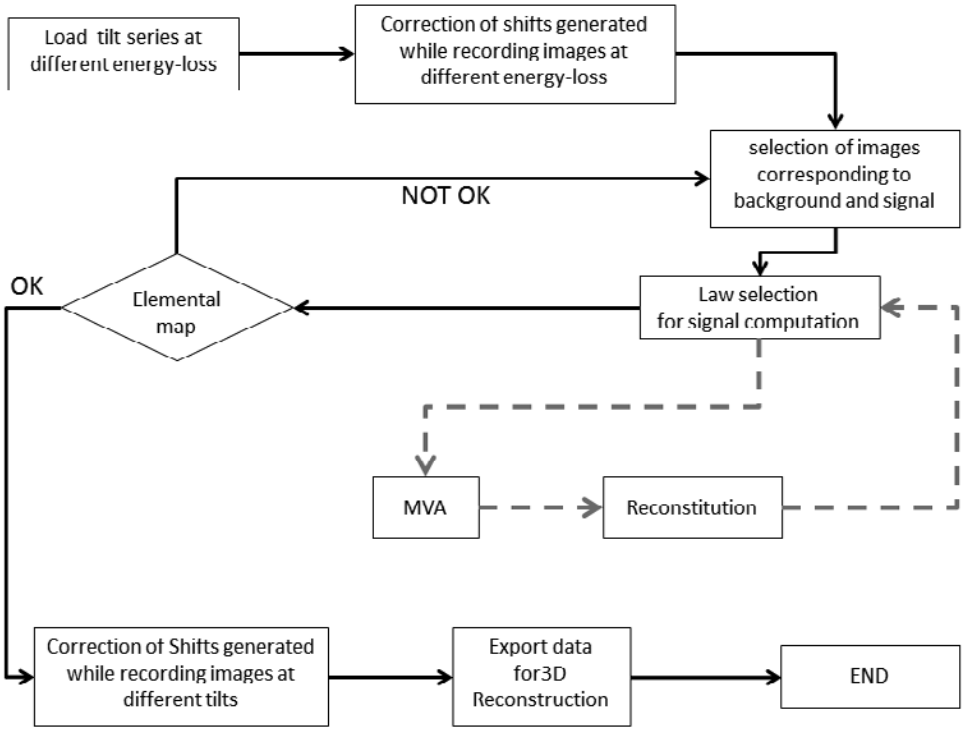

Figure 1. EFTEM-TomoJ workflow. The main steps of the software are described in this chart. Dashed-lined gray loop represents the optional tool for signal-to-noise ratio improvement by principal component analysis. Final tomogram can be computed by any tomographic reconstruction software after exporting the final aligned elemental maps. A manual of the software can be downloaded from http://test.sfbiophys.org/software/update/20130211/Eftem_TomoJ_manual_0.01.pdf.

sition, difference between two images, and the use of reference points.

Another major difficulty in computing accurate EFTEM maps is to choose a correct function for background subtraction to extract the characteristic signal. This choice is based on the physics of electron scattering which can lead to different functions depending on the analyzed element or spectrum region. Thus, EFTEM-TomoJ allows the fitting of the following background models:

Linear: $Y = AX + B$,

Quadratic: $Y = A + BX + CX^2$,

Power: $Y = AX^B$,

Exponential: $Y = Ae^{BX}$,

Logarithmic: $Y = A + B\ln X$,

Log polynomial: $Y = A + B\ln X + C(\ln X)^2$,

Log–log polynomial: $\ln Y = A + B\ln X + C(\ln X)^2$,

where X corresponds to the energy-loss value, Y to the number of counts for each energy, and A, B, and C to the constants calculated for fitting.

The result of applying each model can be quickly visualized by directly plotting the energy counts and values from background function, as well as by the visualization of a regression map where the value of each pixel is the regression coefficient computed for the selected function at the corresponding pixel coordinate. The selected regression model can be applied to the whole image or alternatively to ROI drawn by the user, which leads to an automatic update of the energy counts and background fitted function. Both alignment and selection of function for background subtraction are integrated in a single interface which, in addition to the information indicated, also shows a preview of the resulting map. This aids the selection of alignment and modeling parameters in a visual and intuitive way (Fig. 2).

EFTEM-TomoJ is not limited to the basic three-window method but allows working with as many energy windows as the user wants. This makes it possible to apply powerful methods for statistical noise removal, such as those based on MVA. For this purpose in EFTEM-TomoJ we have implemented PCA, which has previously been used in EFTEM mapping (Quintana et al., 2001). A graphical user interface (Fig. 3) visually guides the user for the choice of eigenvectors during the image reconstitution process by removing undesirable eigenvectors associated with statistical noise. To evaluate the effect of the image reconstitution, this interface shows in real time the resulting map and updates the energy counts and background fitted function plots.

Finally, EFTEM-TomoJ includes a new tomographic reconstruction algorithm (BgART) that produces maps optimized for subsequent segmentation and volume rendering. BgART uses an initial ART/SIRT-reconstructed volume to determine the gray level (M_h) appearing with highest frequency in the image histogram. This value is assimilated to the value of the background. Based on Mh, a dynamic

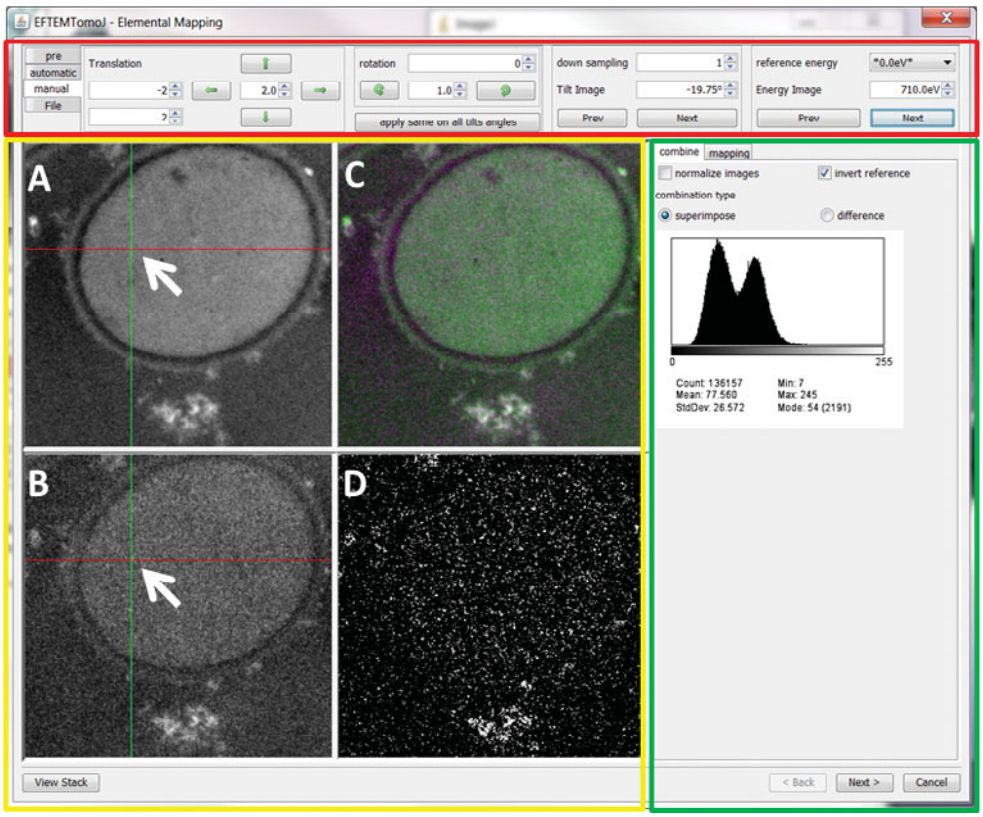

Figure 2. Energy-loss and mapping tools interface. This interface contains the tools allowing alignment of the tilt series acquired at different energy-loss values and computation of elemental maps for each angle. As described in the manual (http://test.sfbiophys.org/software/update/20130211/Eftem_TomoJ_manual_0.01.pdf), the interface is divided in to three main frames. On top the "selection and information frame" (boxed in red in the figure). Here the preprocessing tool (hot-spot removal) together with automatic or manual alignment tools can be selected by clicking the tags at the left of this frame. To recover previous alignments or to save the last one computed for use in the future, the geometric transform matrix can been recorded or loaded using the "file" tag. The right part of the "selection and information frame" is devoted to the choice of images to be displayed in the "image frame" (boxed in yellow in the figure). This "image frame," located at the lower left part of the interface, shows four images. The first three correspond to a reference image (**a**), to an aligned image (**b**), and to the overlapping or difference between the aligned and the reference image (**c**) depending on the selection chosen at the "combine" tag shown at the "command frame" (boxed in green in the figure). The last image of the "image frame" (**d**) shows the resulting elemental map. To facilitate manual alignment, if required, a red and a green line are displayed. These lines intersect at the same coordinate (indicated by arrows in the figure) on the reference and aligned images. The position of this intersection can be changed by using the computer mouse. Finally, the "command frame" (boxed in green in the figure) displays the histogram of the superimposed or difference image depending on the selection of the visualization mode. It also exhibits the "mapping tag" which activates the "map computing interface" detailed in Figure 3.

threshold (T_d) is computed as $T_d = M_h + K\sigma$, where K is defined by the user and σ corresponds to the sample standard deviation. All voxel values lower than T_d are set to M_h, resulting in background equalization. As defined, the correct estimation of T_d needs a higher volume occupied by the background than by the objects. A 3D median filter, with a cross neighborhood radius empirically fixed to 1, is then applied and followed by ART/SIRT reconstruction. Each ART/SIRT iteration performed after background equalization will optimize the contribution of the objects to the reconstructed volume leading to a better definition of details. The stepwise ART/SIRT reconstruction, Mh and Td determination, background equalization, and median filtering are repeated until the user considers the result as satisfactory.

In order to show the application of EFTEM-TomoJ, its use has been evaluated on two samples, one from biological sciences and another from material sciences. In the first one, we have computed iron maps on cells from *F. pedrosoi* using the *Z* loss as reference for alignment. 3D maps with or without use of PCA, followed or not by BgART, are shown in Supplementary Video 1. Central sections of these maps are shown in Figure 4 together with SNR values calculated in cytoplasm and iron aggregates. The iron map without PCA, nor BgART, shows iron aggregates close to the cell wall. Fungal cytoplasm looks similar to resin but without PCA the cell wall makes the cytoplasm more apparent. Nevertheless, the SNR values calculated in the central sections of iron 3D maps before any treatment, after use of

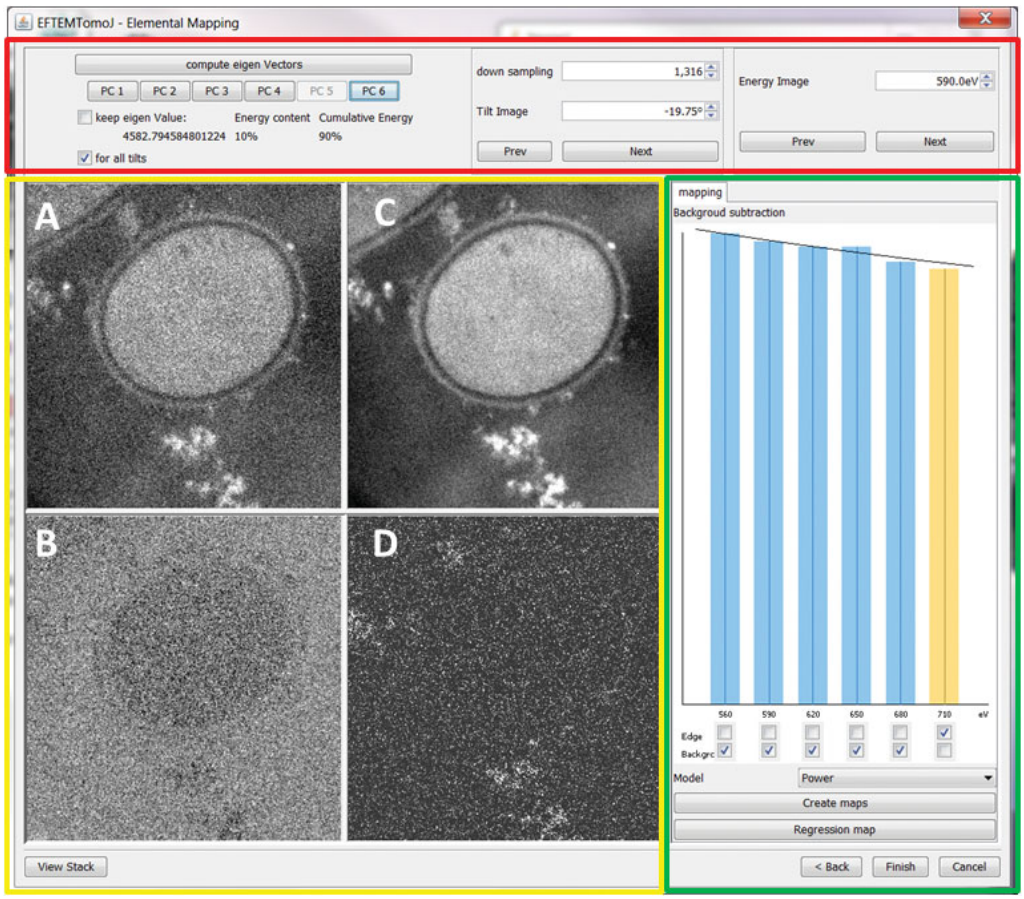

Figure 3. Principal component analysis and mapping tools interface. The aim of this interface is to select the background subtraction function to be used for mapping and to select the eigenvectors for image reconstitution in case that PCA option is used. As was the case for the "energy-loss and mapping tools interface" (Figure 2), it is divided into three frames. On the top the "selection and information frame" (boxed in red in the figure) includes tools for eigenvector selection prior to reconstitution of a whole data set or of a single image (left) and allows selection of the image to be displayed on the "image frame" (boxed in yellow in the image) depending on the choice of energy and tilt values (right). On the bottom left "image frame" (boxed in yellow in the image) displays four images corresponding to the original image (**a**), the selected eigenvector (**b**), the reconstituted image resulting by combining the selected eigenvectors (**c**), and the elemental map (**d**) resulting from the reconstituted images. The right frame (boxed in green in the figure) corresponds to the "mapping tools." This interface is common to the "energy-loss and mapping tools interface" and to the "principal component analysis and mapping tools interface." It shows a bar plot representing the intensity of signal for each energy, computed for the whole image or a region of interest that can be selected on the "image frame" by using the mouse. The length of each histogram represents the dimension of the energy window. Blue bars correspond to images selected as background and yellow bars are those assigned to signal, the selection can be done by checking or unchecking the boxes below each bar. Bars for images that will not be considered for computing background or maps (unchecked boxes) will appear in gray. The bar plot also includes a black line representing the fitting of the selected background subtraction function, which can be chosen in the "model list box" on this frame. This function is computed only with the images selected for background and can be displayed for the whole data set or for a selected region of interest. Once the conditions are chosen, final elemental or regression maps can be created and exported for reconstruction or analysis by clicking on the "created maps" or "regression map" button respectively in this "mapping tools" frame.

PCA, and after PCA followed by BgART, do not evidence any enhancement on the signal (−22, −32, and −21 dB, respectively). This is not the case in iron aggregates where the SNR is improved after PCA (from 1 dB without PCA to 4 dB after PCA) and after PCA followed by BgART (from 1 dB without PCA to 28 dB after PCA followed by BgART). Results on the material science example are shown in Supplementary Video 2. Here, TiO_2 particles were deposited on holey carbon film grids, and O and Ti 3D maps were computed by using carbon images as reference. As was the case on the biological sample, visual comparison of the computed 3D maps shows the interest of use of PCA combined with BgART.

Supplementary Material

To view Supplementary Videos 1, 2, and 3 for this article, please visit http://dx.doi.org/10.1017/S1431927613013317.

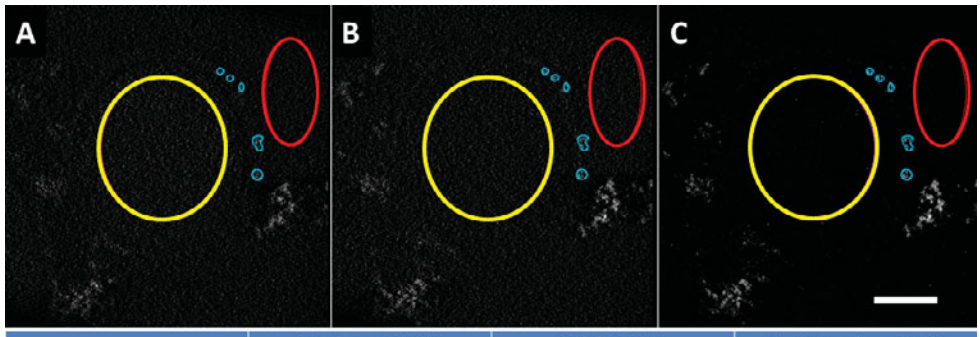

SNR	Without MVA	With MVA	BgART after MVA
cytoplasm	-22 dB	-32 dB	-21 dB
iron	1 dB	4 dB	29 dB

Figure 4. Example of application of the software for the study of iron aggregated on *Fonsecaea pedrosoi*. Images on the top of the figure correspond to the central planes of the iron 3D maps (Supplementary Video 1) before the use of MVA (**A**), after MVA (**B**), and after combining MVA and reconstruction using BgART (**C**). The delimited regions correspond to those used to compute the signal-to-noise ratio (SNR) in cytoplasm (red) and iron around the fungus cell wall (blue) with regard to the resin (red) high was considered as noise. The SNR (expressed in dB) is shown in the table at the bottom of the figure. Scale bar is 400 nm.

Discussion

Electron tomography is a standard procedure for structural analysis in the materials sciences and biology. The combination of transmission electron tomography and chemical mapping by EFTEM complements the structural information obtained by tomography with the 3D localization of studied chemical elements. A TEM capable of tomography and equipped with an in-column energy filter thus becomes a powerful tool for 3D ultrastructural analysis. Despite the data acquisition step of this process being fully automated today, the computation of accurate 3D chemical maps by EFTEM is frequently limited by the absence of a comprehensive workflow and user-friendly implementation of robust algorithms for signal processing, SNR improvement, validation, and analysis. The software presented in this article (EFTEM-TomoJ) addresses this problem and aims to facilitate the computation of 3D chemical maps by EFTEM by nonspecialists. For this purpose, special attention has been paid to develop a user-friendly interface that guides the user in obtaining an accurate final map. In addition, in order to make EFTEM-TomoJ easy to install and available on all operating systems, it has been developed as a plug-in for the popular ImageJ software and is fully compatible with the ImageJ tomography plugin TomoJ. The export of background-subtracted and PCA-denoized image series to any other tomographic reconstruction programs as TIFF files is likewise supported.

The tools implemented in EFTEM-TomoJ allow the user to circumvent a range of drawbacks inherent to 3D chemical mapping by EFTEM. The principle of EFTEM is based on building-up a correct spectrum from the different energy-loss recorded images (image spectra) in which each pixel value corresponds to the spectroscopic information in a defined position. This implies that all the pixels placed at equivalent coordinates in the images at different energies correspond to the same position to reconstitute a coherent spectrum. This means precise alignment of images at the same tilt and different energy loss.

The implementation of multiscale methods has the advantage of a better management of low SNR than a direct alignment without image scaling (Bonnet & Liehn, 1988). This is of interest especially in the case of biological samples, where SNR is often low due to the narrow contrast range between structures and solvent. In addition, the possibility to use mutual information as the scoring function for image alignment as an alternative to classically used functions such as mean square difference and cross-correlation provides a robust tool when important contrast changes occur allowing the use of any energy-loss tilt series (zero loss, plasmon, characteristic signal, pre- or post edge) as reference. Taking into account that zero-loss tilt series frequently correspond to the highest SNR, they are in most cases ideally suited for determining the amount of shift between images recorded at different tilt angles. This information can then later be used to align the maps after background subtraction, which also has the advantage to provide a direct superposition of the chemical 3D map on the standard structural tomogram computed from zero-loss images. In addition to the automatic alignment, a manual alignment graphical tool is proposed by EFTEM-TomoJ allowing the correction of misalignments warranting the use of data with poor SNR, or unsuitable for automated or fiducial-based alignment. Also the visualization of a real-time computed chemical map preview helps in assessment of the alignment by depicting artifacts associated with inaccuracy alignments such as the apparition of duplicated borders in objects.

Concerning the choice of the best function for signal extraction, a drawback (or restriction) of currently available

software for the computation of chemical maps by EFTEM is that they provide only a small number of regression models (in general Egerton or power laws) often limited to three energy-loss windows. While this is sufficient in the case of elements presenting sharp signal peaks, more complex models are often required for mapping elements with weaker or widespread energy-loss signatures, such as phosphorus and many other elements of interest to biologists. The possibility of choosing among six different functions for background subtraction, combined with the option to include post-edge images in the fitting process, can facilitate correct determination of the characteristic signal and hence reduce under- or over-estimation of pixel values. Implementation of different functions for signal extraction as well as a range of qualitative and quantitative evaluation tools is meant to increase user confidence in the results. Thus, in addition to the real-time preview map described above, it is possible to visualize a regression map of the selected function used for background modeling. This map serves both to validate the chosen function for the entire image and to identify regions in which the function fails to model the background signal. In addition to the regression map, the energy-loss values from each image versus the number of counts together with the fitted function are graphically shown. This representation is automatically updated when the function is changed or when an energy-loss window is removed from calculations or re-flagged as signal or background window. This improves accuracy of the computed elemental map by preventing the inclusion of images not fitting with any function used for background modeling. Moreover, because the analyzed element can have a heterogeneous distribution in the sample, the plot can be calculated only in a region of interest defined by the user. This allows local analysis making possible the validation of the selected law and images by checking that no significant characteristic signal appears where the user knows that the mapped element is absent and give positive intensity where present. These tools allow validating the mapping parameters before applying them to the entire tilt series.

However, besides the optimization of characteristic signal extraction by precise alignment and choice of law, a further hurdle appears when a low concentration of the mapped element leads to a low SNR which is frequently the case in biological samples. Enhancement of SNR by mage reconstitution after PCA allows better fitting of the mathematical function for background subtraction and therefore the improvement of final maps. Obviously, this part of the workflow is optional and can be skipped in case the SNR is high enough to provide valid maps with low noise.

Finally, rendering and segmentation of the final 3D chemical map can be difficult because of remaining noise. To this end various methods, including anisotropic or isotropic denoizing in Fourier or real space (Volkmann, 2010), are commonly applied on the reconstructed volume. However, these methods are prone to removal of interesting information associated with details in the reconstructed volume. Recently, other methods taking advantage of iterative reconstruction approaches, such as DART have recently been applied with success in tomography. However, they require prior knowledge about the number of elements to be segmented and their corresponding gray levels. DART is thus better suited for materials sciences where samples are often composed of fewer and more clearly delimited compounds. An approach denoted as partially discrete algebraic reconstruction technique (PDART) has recently been successfully applied to segmentation of nanoparticles (Roelandts et al., 2012). PDART is based on detection of features in the volume based on their voxel intensities, requiring prior information about the number of expected materials. The algorithm implemented in EFTEM-TomoJ, on the other hand, is focused on the detection of the volume background and does not require any prior knowledge of the number of materials existing in the sample. Because background value is fixed for every iteration, it is mainly the voxel intensity of the features that changes during the process. Thus, the intensity recovered for each feature after BgART has a similar level to that obtained with standard ART reconstruction, but the uniform background facilitates segmentation of objects.

On the whole, the possibilities offered by EFTEM-TomoJ are: (i) standard 3D chemical mapping by EFTEM, with and without (ii) noise reduction by PCA, combined or not with (iii) BgART for volume reconstruction. These methods have been successfully used to obtain iron maps from images of the fungus *F. pedrosoi* incubated with cationized ferritin, validating the approach. This pathogenic fungus produces melanin, a dark, phenolic polymer related to virulence. Such pigment is associated with negative charges on the fungal surface. To detect negatively charged areas on the surface, and therefore, areas where melanin is concentrated on the cell wall, the fungus was incubated with iron cationized ferritin, for the observation of iron via EFTEM tomography. As expected, PCA slightly improves localization of the characteristic iron signal as demonstrated by the increment by a factor of 4 in the SNR. This low enhancement on the SNR is highly improved when PCA is followed by BgART because the SNR is multiplied by a factor close to 30 making the direct segmentation of the map more straightforward as shown in Figure 5 and Supplementary Video 3.

Conclusion

The software presented in this work constitutes the first publicly available toolset for 3D chemical mapping by EFTEM (EFTEM-TomoJ), including an extensive number of methods for elemental signal extraction, SNR improvement by MVA, and volume–background suppression during the ART-based reconstruction process. We consider that the user-friendly interface, the robust tools offered in the software, as well as the new algorithm BgART implemented to facilitate volume segmentation, can truly assist the scientific community interested in the 3D localization of chemical elements to generate accurate 3D elemental maps from their samples. Thus, in addition to the example presented

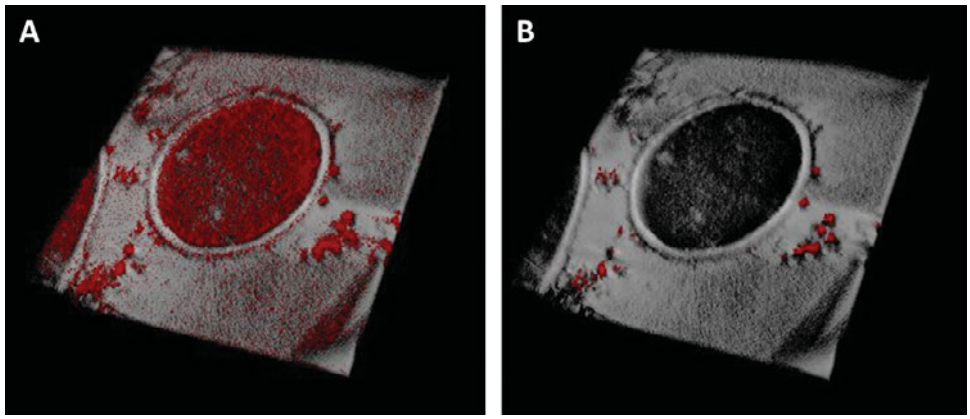

Figure 5. 3D rendering of *Fonsecaea pedrosoi* reconstructed iron 3D maps. Panels show the superposition of the *Z*-loss volume (gray levels) with the iron 3D maps (red) after threshold segmentation (done with the same threshold value: 128 in 8 bits) by using ImageJ 3D-viewer tool. Panel **A** corresponds to the iron 3D map before the use of MVA and panel **B** to the map after combining MVA and BgART.

here, EFTEM-TomoJ is also being used by beta-testers within the materials science community (Florea et al., 2012). EFTEM-TomoJ may be downloaded from http://u759.curie.fr/download/softwares/EFTEM-TomoJ, where a comprehensive user manual and test data set are also available.

Acknowledgments

The authors want to thank Dr. Sonia Rozental from the Universidade Federal do Rio de Janeiro (Brazil) for the kind donation of fungal samples, the "Fondation pour la Recherche Médicale" for the fellowship of MC, and "Region Ile de France" for its contribution to the purchase of the JEOL JEM 2200FS microscope used for every experiment reported in this manuscript. C.O.S. Sorzano is supported by a "Ramón y Cajal" research contract.

References

Aronova, M.A., Kim, Y.C., Harmon, R., Sousa, A.A., Zhang, G. & Leapman, R.D. (2007). Three-dimensional elemental mapping of phosphorus by quantitative electron spectroscopic tomography (QuEST). *J Struct Biol* **160**, 35–48.

Aronova, M.A., Sousa, A.A., Zhang, G. & Leapman, R.D. (2010). Limitations of beam damage in electron spectroscopic tomography of embedded cells. *J Microsc* **239**, 223–232.

Batenburg, K.J. & Sijbers, J. (2011). DART: A practical reconstruction algorithm for discrete tomography. *IEEE Trans Image Process* **20**, 2542–2553.

Bonnet, N. & Liehn, J.C. (1988). Image registration in electron microscopy: Application of a robust method. *J Electron Microsc Tech* **10**, 27–33.

Boudier, T., Lechaire, J.P., Frébourg, G., Messaoudi, C., Mory, C., Colliex, C., Gaill, F. & Marco, S. (2005). A public software for energy filtering transmission electron tomography (EFTET-J): Application to the study of granular inclusions in bacteria from Riftia pachyptila. *J Struct Biol* **151**, 151–159.

Cunha, M.M., Franzen, A.J., Alviano, D.S., Zanardi, E., Alviano, C.S., De Souza, W. & Rozental, S. (2005). Inhibition of melanin synthesis pathway by tricyclazole increases susceptibility of *Fonsecaea pedrosoi* against mouse macrophages. *Microsc Res Tech* **68**, 377–384.

Florea, I., Ersen, O., Arenal, R., Ihiawakrim, D., Messaoudi, C., Chizari, K., Janowska, I. & Pham-Huu, C. (2012). 3D analysis of the morphology and spatial distribution of nitrogen in nitrogen-doped carbon nanotubes by energy-filtered transmission electron microscopy tomography. *J Am Chem Soc* **134**, 9672–9680.

Goris, B., Roelandts, T., Batenburg, K.J., Heidari Mezerji, H. & Bals, S. (2013). Advanced reconstruction algorithms for electron tomography: From comparison to combination. *Ultramicroscopy* **127**, 40–47.

Leapman, R.D., Kocsis, E., Zhang, G., Talbot, T.L. & Laquerriere, P. (2004). Three-dimensional distributions of elements in biological samples by energy-filtered electron tomography. *Ultramicroscopy* **100**, 115–125.

Lozano-Perez, S., de Castro Bernal, V. & Nicholls, R.J. (2009). Achieving sub-nanometre particle mapping with energy-filtered TEM. *Ultramicroscopy* **109**, 1217–1228.

Messaoudi, C., Boudier, T., Sorzano, C.O. & Marco, S. (2007). TomoJ: Tomography software for three-dimensional reconstruction in transmission electron microscopy. *BMC Bioinformatics* **8**, 288–297.

Midgley, P.A. & Weyland, M. (2003). 3D electron microscopy in the physical sciences: The development of Z-contrast and EFTEM tomography. *Ultramicroscopy* **96**, 413–431.

Möbus, G. & Inkson, B.J. (2001). Three-dimensional reconstruction of buried nanoparticles by element-sensitive tomography based on inelastically scattered electrons. *Appl Phys Lett* **79**, 1369–1371.

Pluim, J.P., Maintz, J.B. & Viergever, M.A. (2003). Mutual-information-based registration of medical images: A survey. *IEEE Trans Med Imaging* **22**, 986–1004.

Quintana, C., Lechaire, J.P., Bonnet, N., Risco, C. & Carrascosa, J.L. (2001). Elemental maps from EFTEM images using two different background subtraction models. *Microsc Res Tech* **53**, 147–156.

Quintana, C., Marco, S., Bonnet, N., Risco, C., Gutiérrez, M.L., Guerrero, A. & Carrascosa, J.L. (1998). Optimization of phosphorus localization by EFTEM of nucleic acid containing structures. *Micron* **29**, 297–307.

Roelandts, T., Batenburg, K.J., Biermans, E., Kübel, C., Bals, S. & Sijbers, J. (2012). Accurate segmentation of dense nanoparticles by partially discrete electron tomography. *Ultramicroscopy* **114**, 96–105.

Schneider, C.A., Rasband, W.S. & Eliceiri, K.W. (2012). NIH Image to ImageJ: 25 years of image analysis. *Nat Methods* **9**, 671–675.

Sorzano, C.O., Messaoudi, C., Eibauer, M., Bilbao-Castro, J.R., Hegerl, R., Nickell, S., Marco, S. & Carazo, J.M. (2009). Marker-free image registration of electron tomography tilt-series. *BMC Bioinformatics* **10**, 124–135.

Volkmann, N. (2010). Methods for segmentation and interpretation of electron tomographic reconstructions. *Methods Enzymol* **483**, 31–46.

Yedra, L., Eljarrat, A., Arenal, R., Pellicer, E., Cabo, M., López-Ortega, A., Estrader, M., Sort, J., Baró, M.D., Estradé, S. & Peiró, F. (2012). EEL spectroscopic tomography: Towards a new dimension in nanomaterials analysis. *Ultramicroscopy* **122**, 2–18.